minerals

MDPI

Article

A Mineralisation Age for the Sediment-Hosted Blackbush Uranium Prospect, North-Eastern Eyre Peninsula, South Australia

Urs Domnick [1], Nigel J. Cook [1,*], Cristiana L. Ciobanu [1], Benjamin P. Wade [2], Liam Courtney-Davies [1] and Russel Bluck [3]

[1] School of Chemical Engineering and Advanced Materials, The University of Adelaide, Adelaide, SA 5005, Australia; urs.domnick@adelaide.edu.au (U.D.); cristiana.ciobanu@adelaide.edu.au (C.L.C.); liam.courtney-davies@adelaide.edu.au (L.C.-D.)

[2] Adelaide Microscopy, The University of Adelaide, Adelaide, SA 5005, Australia; benjamin.wade@adelaide.edu.au

[3] Samphire Uranium Pty Ltd., 28 Greenhill Road, Wayville, SA 5034, Australia; rbluck@uraniumsa.com.au

* Correspondence: nigel.cook@adelaide.edu.au; Tel.: +61-405-826-057

Received: 9 November 2019; Accepted: 17 February 2020; Published: 20 February 2020

Abstract: The Blackbush uranium prospect (~12,580 tonnes U at 85 ppm cut-off) is located on the Eyre Peninsula of South Australia. Blackbush was discovered in 2007 and is currently the single example of sediment-hosted uranium mineralisation investigated in any detail in the Gawler Craton. Uranium is hosted within Eocene sandstones of the Kanaka Beds and, subordinately, within a massive saprolite derived from the subjacent Hiltaba-aged (~1585 Ma) granites, affiliated with the Samphire Pluton. Uranium is mainly present as coffinite in different lithologies, mineralisation styles and mineral associations. In the sandstone and saprolite, coffinite occurs intergrown with framboidal Fe-sulphides and lignite, as well as coatings around, and filling fractures within, grains of quartz. Microprobe U–Pb dating of coffinite hosted in sedimentary units yielded a narrow age range, with a weighted average of 16.98 ± 0.16 Ma (343 individual analyses), strongly indicating a single coffinite-forming event at that time. Coffinite in subjacent saprolite generated a broader age range from 28 Ma to 20 Ma. Vein-hosted coffinite yielded similar ages (from 12 to 25 Ma), albeit with a greater range. Uraninite in the vein is distinctly older (42 to 38 Ma). The 17 ± 0.16 Ma age for sandstone-hosted mineralisation roughly coincides with tectonic movement as indicated by the presence of horst and graben structures in the Eocene sedimentary rocks hosting uranium mineralisation but not in stratigraphically younger sedimentary rocks. The new ages for hydrothermal minerals support a conceptual genetic model in which uranium was initially sourced from granite bedrock, then pre-concentrated into veins within that granite, and is subsequently dissolved and reprecipitated as coffinite in younger sediments as a result of low-temperature hydrothermal activity associated with tectonic events during the Tertiary. The ages obtained here for uranium minerals within the different lithologies in the Blackbush prospect support a conceptual genetic model in which tectonic movement along the reactivated Roopena Fault, which triggered the flow of U-rich fluids into the cover sequence. The timing of mineralisation provides information that can help optimise exploration programs for analogous uranium resources within shallow buried sediments across the region. The model presented here can be predicted to apply to sediment-hosted U-mineralisation in cratons elsewhere.

Keywords: uranium mineralisation; Eyre Peninsula; Blackbush uranium prospect; U–Pb microprobe geochronology; Kanaka Beds; coffinite

1. Introduction

South Australia has long been recognised as being exceptionally well endowed with uranium resources. All currently economically relevant deposits are associated with high-U Mesoproterozoic felsic rocks [1]. In the Gawler Craton, iron-oxide copper-gold (IOCG) deposits are genetically related to the emplacement of Hiltaba Suite granites at ~1.6 Ga [2,3]. The supergiant Olympic Dam IOCG(U) deposit contains the largest known U resource of any uranium deposit on Earth but is primarily a copper producer with by-product U [4]. In the Curnamona Province, in the east of South Australia, sediment-hosted U deposits, like the current operating mines Beverley and Four Mile, are widespread and source their U from granites and metavolcanics of the Mesoproterozoic Ninnerie Supersuite [1].

Considering the extent of Mesoproterozoic Hiltaba-affiliated bedrock granites [5] and organic-rich sediments across the Gawler Craton (e.g., [6]), similar to those hosting U in the Curnamona Province, large sediment-hosted deposits would be expected. The Blackbush uranium prospect, located on the north-eastern Eyre Peninsula, South Australia (shown on the bedrock map included here as Figure 1) is, however, currently the only example of sediment-hosted U mineralisation in the Gawler Craton that has been investigated in any detail. Blackbush was discovered in 2007 by UraniumSA, a junior exploration company, who recognised the Kanaka Beds as highly prospective for U. The first drill hole intersected a roll front, which culminated in the discovery of Blackbush in 2007 [7], and shortly afterward, the discovery of the geologically similar Plumbush resource.

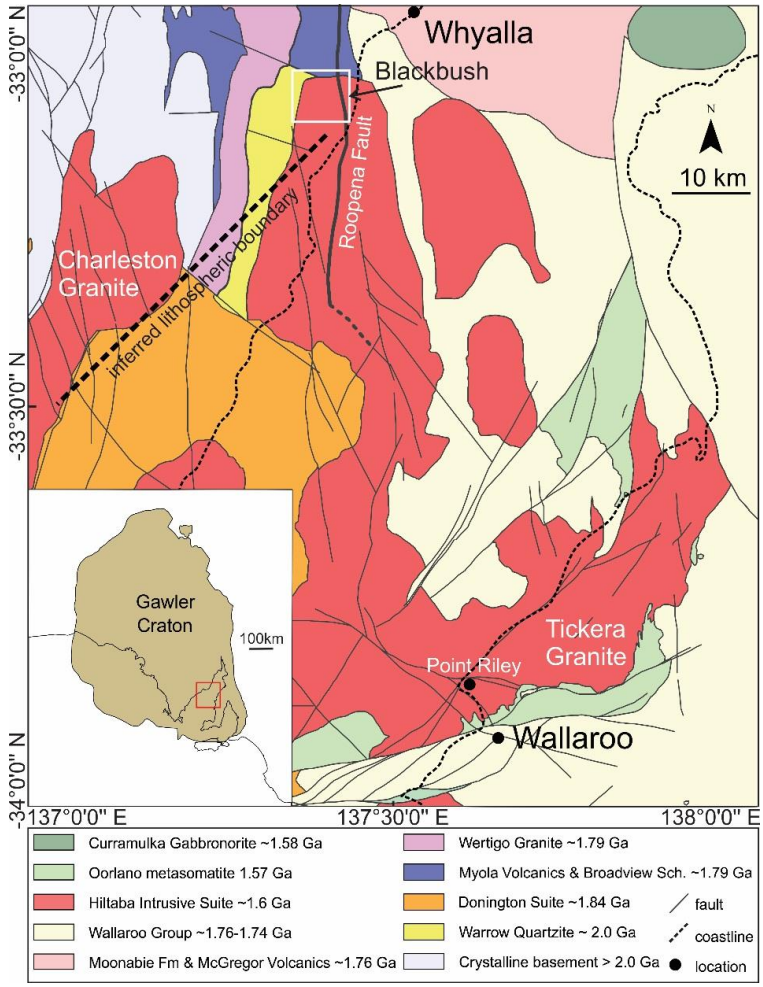

Figure 1. Simplified geological map of bedrock in the north-eastern Eyre Peninsula, Spencer Gulf and adjacent areas, with the location of Blackbush marked. Inset map locates the area within the Gawler Craton. Map based on unpublished material of Samphire Uranium Ltd.

In the Blackbush prospect, uranium is mainly hosted within Eocene siliciclastic sediments of the Kanaka Beds that fill a palaeochannel at the unconformity with subjacent granites of the Samphire pluton, affiliated with the Hiltaba Intrusive Suite. Domnick et al. [8] described the geological setting of the Samphire uranium resource, with emphasis on the geochemistry, mineralogy and alteration of granite bedrock. Three geochemically distinct granite types were identified in the Samphire Pluton [8] and correspond to domains interpreted from geophysical data [9]. All granites show complex chemical and textural alteration overprints which increase in intensity closer to Blackbush, as well as crosscutting veins [8]. Furthermore, all three granite types are anomalously rich in U relative to crustal averages [8]. The highly variable Th/U ratios (from 0.8 to 11.9), as well as the presence of hydrothermal U minerals (mostly coffinite) within all the Samphire granites and crosscutting veins were arguments favouring U mobility [8], leading to the hypothesis that cover-bound uranium was sourced from these granites. In the conceptual model for the mineralisation presented by [8], the uranium was proposed to be pre-concentrated in veins in the upper parts of the pluton during a temporally unconstrained event post-dating Proterozoic granite emplacement. Uranium was then leached and migrated upwards after deposition of the Paleogene and Neogene sedimentary cover above an unconformity that represents a gap of more than 1.5 Ga. Despite the spatial link between mineralisation and a major unconformity, Blackbush cannot be classified as an unconformity-related U deposit. This is due to a lack of conspicuous features associated with such deposits (high grade, highly saline brines, graphitic lithologies in the basement, the dominance of uraninite over coffinite, etc., e.g., [10]).

The objective of the present work is to obtain an accurate age for coffinite-dominant uranium mineralisation in the Blackbush resource, using the chemical (microprobe) age method of Bowles [11,12]. Geochronology is focussed on coffinite within the Kanaka Beds and forming the major part of the mineralisation but also in saprolite at the unconformity, as well as uraninite within granite-hosted veins immediately below. The aim was to expand the geochronological framework for the mineralisation and further validate the genetic model. An accurate age for mineralisation relative to host rock is also considered an important contribution to an exploration model applicable to the search for analogous uranium mineralisation in the region.

2. Geological Setting

2.1. Granite Bedrock

The bedrock to the Blackbush prospect is the Samphire pluton. In a petrographic study of the pluton and its relationship with uranium mineralisation in the suprajacent cover sequence, Domnick et al. [8] recognised three distinct granitoids forming the Samphire Pluton. The southern part of the pluton was informally called the green granite (Granite B) [8]. The same terminology is applied here for the sake of consistency. The northern part, immediately underlying the Blackbush mineralisation, comprises a red granite (Granite C), using the nomenclature of [8]. This is characterised by reddened feldspars, high U content, and highly heterogeneous Th/U ratios (~1 to ~10) [8]. The intensity of alteration and density of fractures and veins are increasingly abundant closer to the mineralisation. Granites B and C are separated by an arcuate domain of the so-called yellow granite (Granite A). The latter features higher CaO, and lower U content, prompting [8] to consider it may be significantly less evolved than the other two. In a subsequent publication, Domnick et al. [13] provide new SHRIMP U–Pb zircon ages for each of the three granites, unequivocally linking them to the ~1.6 Ga Hiltaba Intrusive Suite. Granite B yielded an age (weighted averages) of 1585 ± 9 Ma, Granite C 1579 ± 9 Ma, and Granite A 1588 ± 9 Ma; these data showing no statistical difference in age and overlap with U–Pb zircon ages obtained previously [14]. Petrographic observation and geochemical analysis [8,13] support a hypothesis involving late magmatic enrichment of U in the upper part of the pluton, and subsequent leaching of this U in the Paleogene.

2.2. Saprolite

The uppermost part of the granite is weathered to a massive saprolite 10–30 m in thickness [15]. Sodium and potassium are strongly decreased (<0.5 wt.%) relative to fresher granites. Feldspars have been replaced by kaolinite and minor illite, and biotite by kaolinite and rutile (possibly 'leucoxene'). The REE content of the saprolite is variable, several samples display chondrite-normalised REE fractionation patterns that are readily recognisable as compatible with an igneous origin, while other samples have strongly decreased REE with positive Ce-anomalies, as is typical for saprolite and lateritic profiles from a range of settings [16]. In the underlying granite, the magmatic light rare earth element (LREE) mineral is allanite, which is often replaced by either REE-fluorocarbonates or monazite. Monazite and xenotime are unaffected by weathering, whereas samples originally containing REE-fluorocarbonates or allanite have lost significant portions of their REE budget, except for insoluble Ce^{4+} [17].

The saprolite can be separated into three subunits [13], the lowest part of the saprolite is, like the strongly oxidised granite immediately underneath, coloured red by dispersed hematite, the middle unit is yellow and limonitic, whereas the upper unit is white-grey 'reduced' saprolite with minor pyrite. The boundaries between the units are sharp. In drillhole logs made available by UraniumSA Ltd., saprolite is defined as argillaceous brittle granitoid, which is applied to samples with as low as 10% clay. In a typical drill core, the log notes ~30 m of saprolite, the upper half is clay-dominant and the lower half feldspar-dominant. In the clay-dominant part, the uppermost ~10 m are reduced saprolites, followed downwards by ~2.5 m of limonitic saprolite and ~2.5 m of haematitic saprolite [15]. The feldspar dominant part is always hematite-bearing. Relationships between granite, saprolite and overlying lithologies are illustrated in Figure 2.

2.3. Cainozoic Sedimentary Rocks

The saprolite is overlain by the Kanaka Beds, which are widespread siliciclastic sediments of Eocene age in the Pirie Basin and have been considered as lagoonal-estuarine to lacustrine in origin [13], in accordance with regional-scale studies, notably [6]. Blackbush lies on the western edge of the basin (Figure 3). Here, the Kanaka Beds are fluviatile to marine delta sediments and confined to a palaeochannel incised into the granite [15]. The sediments are well-sorted and show upwards-fining or upwards-coarsening cycles. The grain size varies from clay to pebbles. All units in the Kanaka Beds contain organic material and finer grain size correlates with increased organic material, several upward-fining cycles are topped by lignite. The unconformity between the Eocene sediment and the saprolite is marked by a basal conglomerate, the lowest stratum of the Kanaka Beds.

The Kanaka Beds are followed up-sequence by coarse-grained, fossiliferous sand of Melton Limestone affiliation, overlain by carbonate dominated units of the Melton Limestone. Locally, clay is interbedded in sand and carbonates. The Pliocene clays of the Gibbon Beds separate the Melton Limestone from Quaternary soil. The relative timing of sedimentation is constrained from palynological data [18]. Two samples collected from carbonaceous clay and considered to represent the waning stages of sedimentation of the Kanaka Beds in the palaeochannel contained spores and pollen belonging to the *Middle Nothofagidites asperus* zone. This denotes an age of middle to late Eocene and gives an approximate upper age limit for the Kanaka Beds. A sample of lignite collected ~15 km south of Blackbush from the lowest unit of the Kanaka Beds contained the spore-pollen-zone of *Lower Nothofagidites asperus*, giving a rough lower age limit of Middle Eocene [18].

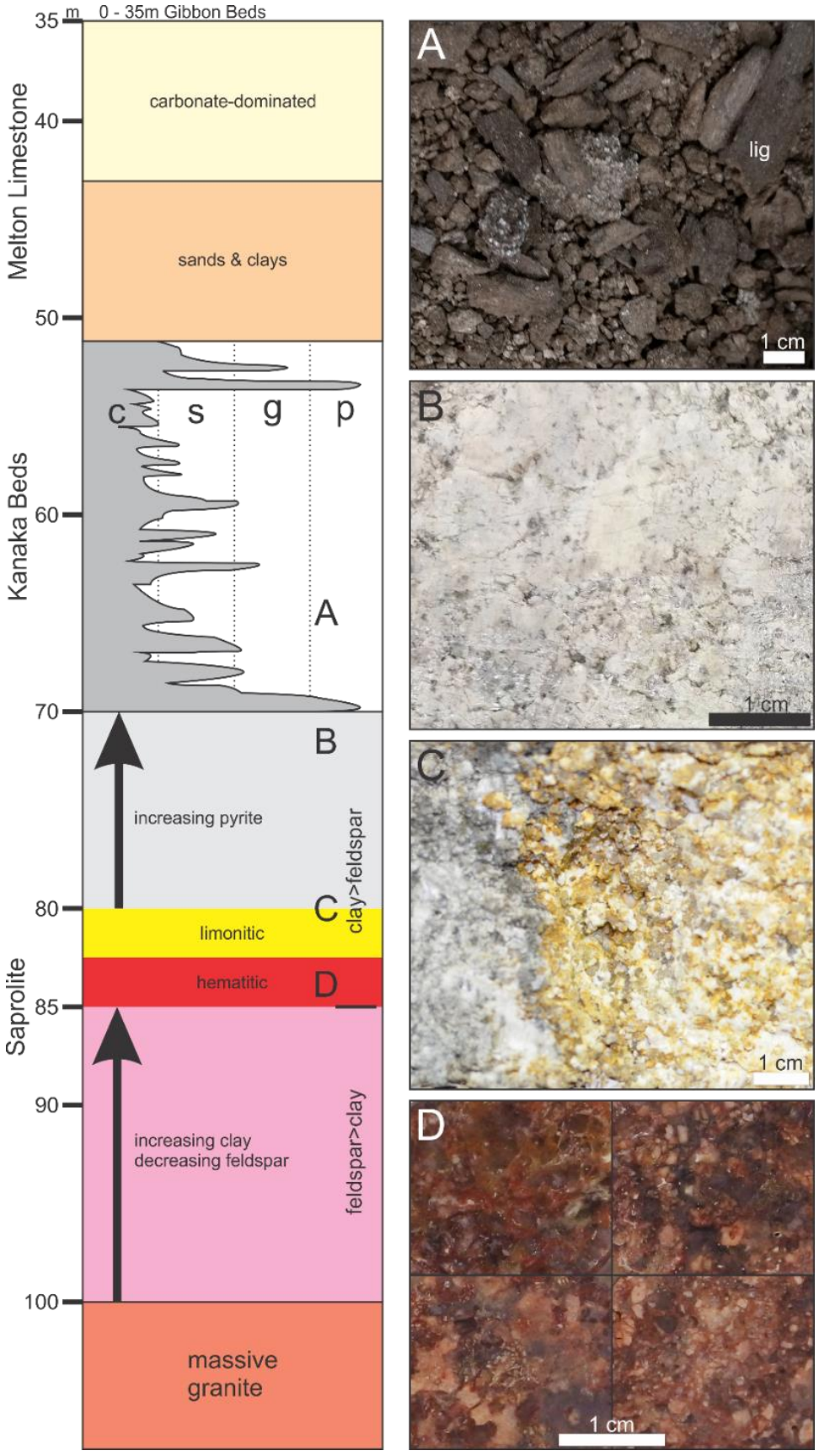

Figure 2. Simplified stratigraphic sequence through the Blackbush resource, with key lithologies indicated. (**A**) Kanaka beds (sands, lignite fragments, clay-dominant clasts); (**B**) reduced saprolite; (**C**) boundary between reduced and limonitic saprolite; (**D**) red saprolite.

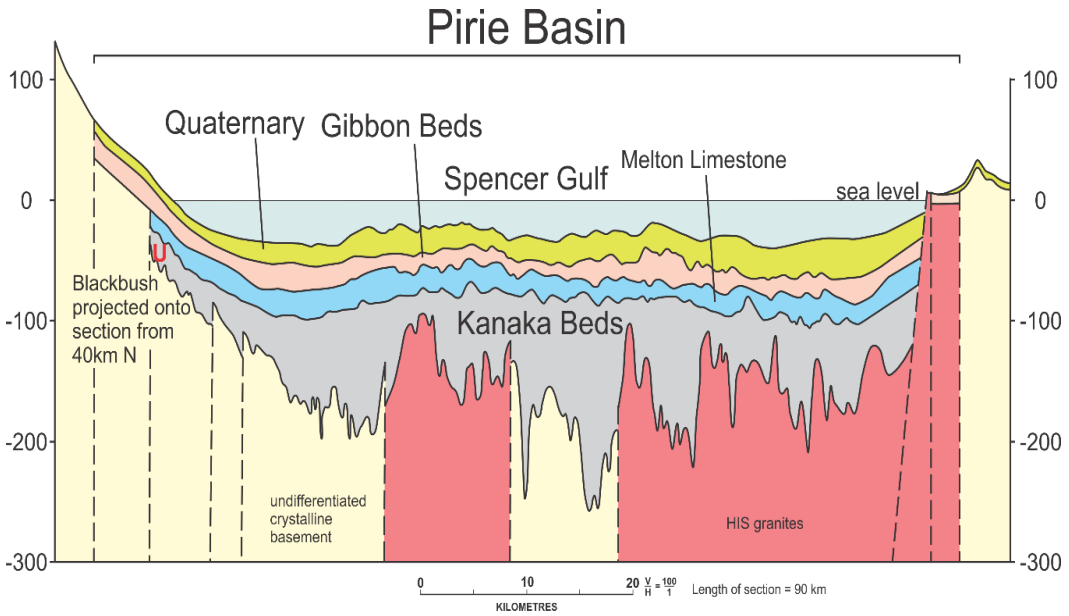

Figure 3. W-E profile of the Eyre Peninsula across the Spencer Gulf (through Point Riley, shown in Figure 1) showing the distribution of Kanaka Beds above a compartmented basement. The vertical scale (in metres) is exaggerated. Adapted from [6].

All rock units in the Blackbush area are affected by tectonic movement, as two fault systems intersect. The Roopena Fault, 6 km east of Blackbush, is a major N-S-striking lithospheric boundary, interpreted as an ancient palaeosuture. Previously considered to be ~1730 Ma in age, newer research points to an age of at least >1850 Ma, most likely >2500 Ma, with reactivation during every major orogeny. Subordinate branches of the Roopena Fault crosscut the bedrock in the Blackbush area (e.g., [19]). In addition, the Pirie Basin is undergoing subsidence since the late Miocene (~10 Ma) with the basement separating into fault blocks creating horst and graben structures. The placement of the palaeochannel hosting the Blackbush mineralisation is controlled by faults.

2.4. Uranium Mineralisation

The style of uranium mineralisation at Blackbush is diverse. Approximately 23% of the U is hosted in the saprolite, mostly stratabound along the unconformity, and to a lesser degree, discordant along faults but always restricted to the reduced saprolite. Approximately 75% is hosted within the Kanaka Beds, along the unconformity, in tabular to lenticular bodies (Figure 4) hosted within the sand, clay, or lignite, and to a small degree, as a roll front like structure. The Kanaka Beds are always organic-rich and reduced. A very small part of the U (~2%) extends into the overlying Melton Limestone sand [15].

The main U mineral is coffinite, $USiO_4$ nH_2O, where $0 < n < 2$ [20], which occurs associated with framboidal pyrite or is present as intergrowths with pyrite or clay minerals. Coffinite and traces of uraninite can also be found in hematite-coffinite-bearing veins that crosscut the underlying granite.

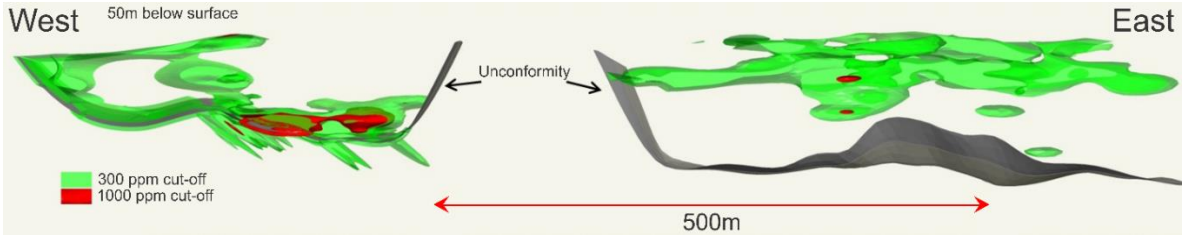

Figure 4. Schematic, simplified NW-SE three-dimensional model of eastern and central parts of the Blackbush prospect, modified after [15] and reproduced with permission.

3. Sampling and Methodology

3.1. Samples

The main objective of this study was to acquire ages for coffinite and other minor U–(Th)-minerals in different lithologies, including the mineralised sandstone, hydrothermal veins in the underlying fresh granite, and material from the saprolitic granite separating both units. The vein and saprolite samples are part of a larger sample suite and were chosen based on the presence of coffinite and subordinate uraninite. The samples representative of uranium mineralisation within the Kanaka Beds consist of nodules hosting intimately intergrown assemblages of pyrite and coffinite, as well as lignite pieces containing coffinite in pores, they were chosen based on their high U content measured via handheld XRF and ease of preparation, taking care to avoid any loss of easily soluble U minerals. All material was mounted in epoxy within one-inch blocks that were polished and consequently examined on an FEI Quanta 450 FEG scanning electron microscope in backscatter electron (BSE) mode located at Adelaide Microscopy (The University of Adelaide, Adelaide, Australia), prior to quantitative microanalysis.

3.2. EPMA Methodology

Chemical ages were acquired using a Cameca SX-Five electron probe microanalyser located in the same laboratory. Chemical compositions of coffinite and other minerals were obtained using a Cameca SX-Five Electron Probe Microanalyser (EPMA) running 'Probe for EPMA' software. All elements were analysed at 15 kV with a defocussed spot of 5 μm. Calcium, Ce, Fe, Si, P, and Th were all initially acquired using a beam current of 40 nA, and once complete, the beam current was automatically turned up to 100 nA for measurement of Pb. EPMA chemical dating studies routinely use beam currents of at least 100 nA to measure Pb.

X-ray lines and standards used were as follows: Ca Kα (plagioclase), U Mβ (synthetic UO_2), Ce Lα ($CePO_4$), Fe Kα (almandine), Si Kα (albite), P Kα (YPO_4), Th Mα (huttonite), Pb Mβ ($PbSiO_3$), and Y Lα (YPO_4). Peak counting times used were 15 s for U and Ce, 25 s for Ca, Fe, Si, and P, 30 s for Th and Y, and 50 s for Pb.

Due to the need to attain the best possible precision on Pb measurements, Pb Mβ was acquired on large PET crystals on three separate spectrometers. The Probe for EPMA software (distributed by Probe Software Inc., Eugene, OR, USA) used allows for aggregation of identical X-ray lines in which the peak-background signal intensities are summed from multiple spectrometers, then fed through the typical φ(ρz) corrections. The lead concentrations obtained when spectrometers were summed/aggregated were compared to resultant individual concentrations when each spectrometer was treated individually, and in all cases, the resultant concentration of summed spectrometers fall well within the error of individual spectrometer concentrations.

All background interpolations utilised linear 2-point backgrounds, with counting times set at 20 s for Ca, U, Ce, Fe, Si and P, 30 s for Th and Y, and 50 s for Pb. Oxygen was calculated by stoichiometry, assuming that all Fe occurs as Fe^{2+}. Matrix corrections of Armstrong-Love/Scott φ(ρz) [21] and Henke MACs were used for data reduction. The Mean Atomic Number correction was utilised for background subtraction (e.g., [22,23]). The average minimum detection limits, in wt.%, were: Ca (0.015), U (0.055), Ce (0.029), Fe (0.023), Si (0.013), P (0.011), Th (0.034), Pb (0.018), and Y (0.021). These detection limits are similar or better than those obtained in other chemical dating studies (e.g., [24]).

3.3. Data Processing

3.3.1. Contamination and Analytical Totals

The very fine-grained nature of the intergrowths of coffinite and pyrite/lignite in the sediment, and coffinite/uraninite and hematite in the vein impedes the acquisition of compositional data that is guaranteed free of any contamination. Calcium is commonly used as an indicator of alteration and associated Pb loss for the chemical dating of monazite or uraninite.

For our sample set, we chose measured iron concentrations as a proxy to identify mixed measurements that include sulphides. Contamination from Fe sulphides shifts ages to the older side, due to their minor Pb content. Any other contamination from other admixed phases does not appear to directly distort ages, but the effect of diluting U and Pb increases the scatter and errors of ages. To avoid this, each analysis of coffinite and thorite with >4 wt.% FeO or >30 wt.% SiO_2 was excluded from further consideration. For uraninite, this limit was increased to 6 wt.% FeO.

Analytical totals for coffinite (sum of all elements in wt.% oxide; Supplementary Materials) are relatively low, as is typical for this microanalytically challenging mineral (e.g., [25]). We explain this as follows. Firstly, this is the result of the presence of molecular water, with the formula of coffinite often given as $USiO_4 \cdot nH_2O$ [20] with an n value equal to 2, rather than $U(SiO_4)_{1-x}(OH)_{4x}$. A composition of $USiO_4 \cdot 2H_2O$ would correspond to a measured total of 90 wt.%, including 74 wt.% UO_2 and 16 wt.% SiO_2, with the 'missing' 10% assigned to H_2O. Secondly, poor totals correspond to elements not analysed, e.g., REE or S, although we do not believe this is ever more than 2–3 wt.%. Thirdly, and in our opinion, the overwhelming reason for poor totals is the nature of the coffinite, with abundant pore spaces and voids, an issue further compromised by small grain size.

Analyses of the dense coffinite used in this study yield totals in the range from 75 up to 93 wt.%, on average 85 wt.%. Totals below 75 wt.% were discarded. For highly porous coffinite analysed in this study, analytical totals were never higher than 79 wt.%. Analyses with totals between 50 wt.% and 79 wt.% have element ratios (and thus ages) identical to those of coffinite with high totals and are interpreted as containing voids and/or anomalously high H_2O content. All analyses with totals below 50 wt.% were discarded. These are mostly non-stoichiometric and compromised by contamination from minerals that contain non-analysed elements, such as Ti in rutile. Analytical totals for uraninite are between 72 and 81 wt.%.

Mineral formulae have not been calculated from the EPMA data and no attempt has been made to charge balance due to the number of unknowns and uncertainties, including but not restricted to the presence of molecular H_2O, the presence of pores and voids, non-analysed elements, and multiple oxidation states of U, Fe, and other elements. Each of these variables will impact the data in similar ways and their effects cannot be readily distinguished. Formulae calculations for U-minerals can be plagued by assumptions (e.g., [26]) that may be difficult or impossible to confirm without access to ultra-sensitive techniques (e.g., [27]). Despite these concerns, or the lack of the complete set of REE or Al, we are confident that precise geochemistry is not needed for chemical dating.

In total, 607 spots were analysed of which 421 (~70%) remained after quality control and processing. Of these, 343 are analyses of coffinite in the nodules of intergrown pyrite-coffinite described above. The balance is made up of 4 analyses of *uranothorite* in the saprolite, 7 spots of coffinite in the saprolite, 8 uraninite in the vein, and 59 coffinite in the vein.

3.3.2. Ages and Uncertainties

Ages were calculated iteratively using the general, widely applied age formula as defined and given by Montel et al. [28]. Although initially used to date monazite, in which U is at comparatively low levels, the formula is widely used in chemical U–Th–Pb dating studies via EPMA, and is identical to that given for minerals containing essential uranium (e.g., [11,12,24,29]) and can be used for any other U-bearing mineral that retains radiogenic Pb, irrespective of concentrations.

In the age equations used, ^{238}U refers to the atomic weight of *U* (and not the specific isotope, ^{238}U). The typical radioactive *Pb* isotopic composition can be expressed as:

$$^{208}Pb = {}^{232}Th\left(e^{\lambda_{232}t} - 1\right) \quad (1)$$

$$^{206}Pb = {}^{238}U\left(e^{\lambda_{238}t} - 1\right) \quad (2)$$

$$^{207}Pb = {}^{235}U\left(e^{\lambda_{235}t} - 1\right) \quad (3)$$

Therefore, the total *Pb* content of a mineral can be expressed as:

$$Pb = {}^{232}Th\left(e^{\lambda_{232}t} - 1\right) + {}^{238}U\left(e^{\lambda_{238}t} - 1\right) + {}^{235}U\left(e^{\lambda_{235}t} - 1\right) \quad (4)$$

Following the fact that we cannot measure isotopes of uranium via EPMA, only total *U*, we can utilise the natural uranium ratio of $^{235}U/^{238}U = 1/138.88$ in order to work out the contribution of measured *Pb* from each isotope of uranium as expressed below:

$$Pb_{conc} = \frac{Th_{conc}}{232} \times \left(e^{\lambda_{232}t} - 1\right) \times 208 + \frac{U_{conc}(0.9928)}{238.04} \times \left(e^{\lambda_{238}t} - 1\right) \times 206 + \frac{U_{conc}(0.0072)}{238.04} \times \left(e^{\lambda_{235}t} - 1\right) \times 207 \quad (5)$$

in which the denominators are the atomic weights of Th and U (i.e., 232 and 238.04, respectively), and the multiplicative values of ^{208}Pb, ^{206}Pb, and ^{207}Pb are the atomic weights of the respective Pb isotopes. Equation (5) represents the chemical dating "age equation", in which all input concentrations are in ppm, and which are then subsequently converted into atomic proportions. This equation is then solved iteratively for *t* (time) until a solution is reached.

For the propagation of uncertainty in any function $w = f(x,y,z)$, the following formula applies, assuming the variables *x*,*y*,*z* are independent:

$$\sigma_w{}^2 = \left(\frac{\delta f}{\delta x}\right)^2 \sigma_x{}^2 + \left(\frac{\delta f}{\delta y}\right)^2 \sigma_y{}^2 + \left(\frac{\delta f}{\delta z}\right)^2 \sigma_z{}^2 \quad (6)$$

Following [30], uncertainties used here have been calculated using peak and background counts, corrections for interference, ZAF etc. This can be applied to the age formula of [28], which can be generalised as $Pb = f(U,Th,t)$. Transforming the formula to acquire the unknown age error (σ_t) results in:

$$\sigma_t = \sqrt{\frac{\sigma_{Pb}{}^2 - \left(\frac{\delta f}{\delta U}\right)^2 \sigma_U{}^2 - \left(\frac{\delta f}{\delta Th}\right)^2 \sigma_{Th}{}^2}{\left(\frac{\delta f}{\delta t}\right)^2}} \quad (7)$$

Theoretically, this formula implies that 'worse' measurements of *U* and *Th* with higher uncertainties would lead to smaller age errors. In practice, all terms are very small compared to σ_{Pb}, and $\frac{\sigma Pb}{Pb} \approx \frac{\sigma t}{t}$. Although we did not include decay constant errors, all calculated ages and errors were crosschecked using precise explicit approximations of [30], which includes decay constant errors. Incorporation of systematic decay constant errors into the uncertainty propagation is not typically done for chemical dating via EPMA, predominantly due to the (relatively) imprecise nature of the chemical EPMA dating technique. Ages and errors of both methods are identical within the given precision. All weighted averages were calculated offline in Isoplot v4.15 [31].

4. Results

4.1. Petrography of Analysed Samples

4.1.1. Granite-Hosted Vein

The granite is medium-grained and weakly fractured. Most igneous minerals are partially or totally altered to secondary assemblages. Plagioclase and orthoclase have been replaced by red albite and K-feldspar, all igneous Fe^{2+}-containing minerals are replaced, e.g., biotite by chlorite, magnetite by hematite, allanite by REE-fluorocarbonates or monazite. This granite has been extensively described previously [8]. Several sections of drill core are dominated by mm- to cm-scale veins and fractures within brecciated granite. Representative of such intervals sampled for the present study are veins with a characteristic silverish to dark grey colour and highly porous filling material (Figure 5A). This

comprises hematite (grains of 10 to 50 µm width), coffinite, quartz, and traces of uraninite (Figure 5B). Coffinite is extremely fine-grained and spherical to colloform in morphology (Figure 5C). Uraninite is only present in trace amounts and occurs as intergrowths with hematite (Figure 5D).

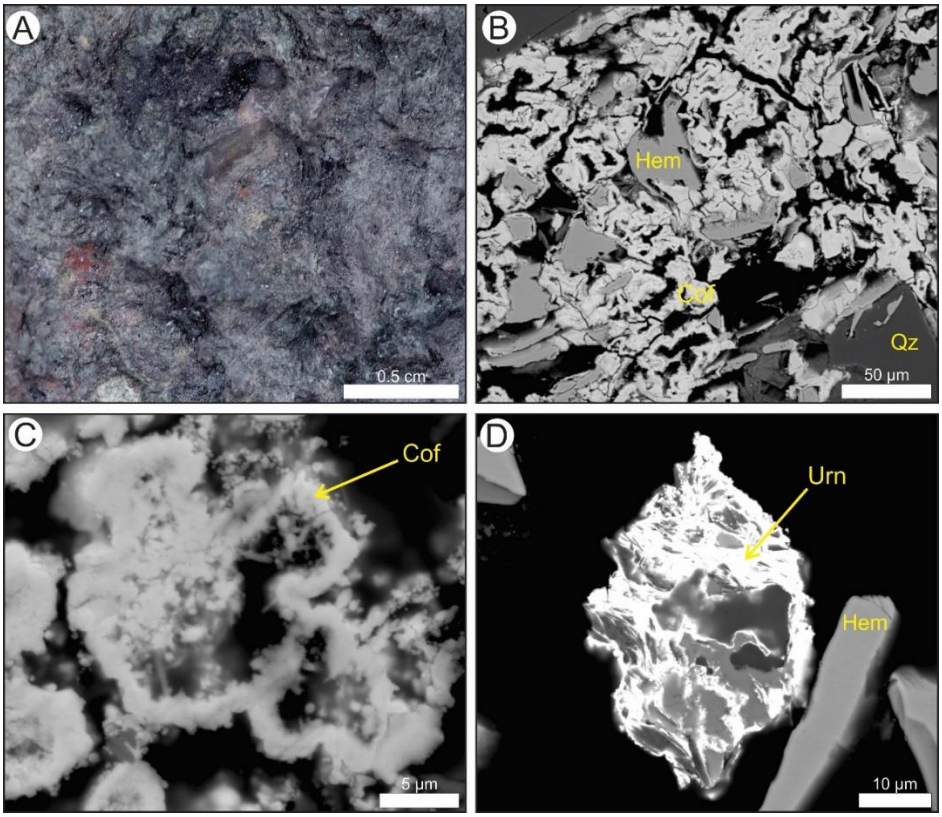

Figure 5. (**A**) Hand specimen photograph of hematite (Hem) + coffinite (Cof) + quartz (Qz) assemblage filling a vein in altered granite. (**B**–**D**) BSE images showing the intimate association between U-minerals and hematite within the vein in (A). Both coffinite and minor uraninite (Urn) are present as sub-micron, fine-grained, colloform aggregates forming rims around hematite laths, quartz grains or filling cavities.

4.1.2. Saprolite

The dated samples are from the uppermost interval comprising reduced saprolite. They contain kaolinite, quartz, pyrite (~1%), and accessory minerals like coffinite, thorite or zircon. The latter four minerals are often associated, thorite or zircon are embedded into framboidal pyrite, coffinite forms either an overgrowth on pyrite or impregnates pyrite and thorite/zircon. The dated minerals in the saprolite, *uranothorite* and coffinite are from these associations.

4.1.3. Sediment-Derived Samples

The lignite pieces are highly variable in size between 0.5 and 2 cm, always black and of irregular shape. The coffinite sits in small cavities in the lignite. The pyrite nodules are 0.2 to 1 cm in size. Although a minority of the nodules are pyrite dominant, shown in the example in Figure 6, the main component is often quartz within which fine-grained pyrite and coffinite are concentrated within fractures (Figure 7).

4.2. Composition of Dated Minerals

In the nodules dominated by pyrite or lignite, the coffinite yielded mostly analytical totals over 80 wt.%, with an average of 85 wt.%. A minority of points have lower totals. These analyses have the same element ratios as higher total analyses, indicating either contamination by non-analysed elements,

or more likely pores and voids. The coffinite is typically poor in minor and trace elements and on average contains 64 wt.% UO_2 and 17 wt.% SiO_2. Thorium is almost always below the minimum limit of detection (~350 ppm) and rarely reaches 400 ppm. Ce_2O_3 is around 0.4 wt.%, Y_2O_3 can reach up to 1.2 wt.% but is mostly very low, rarely below minimum limit of detection. On average the samples contain 1.4 wt.% CaO, although in four analyses it exceeds 3% with a maximum of 9 wt.%. This high CaO does not correlate with increased concentrations of other elements and the analytical totals are within acceptable ranges—only UO_2 seems to be slightly lower, and the higher CaO is interpreted as increased substitution of U by Ca. FeO, wherever present, is always contamination and, on average, around 0.8 wt.%; values > 4.0 wt.% were excluded. P_2O_5 is always < 1.0 wt.%.

Analytical totals of vein coffinite are consistently low in comparison (50–72 wt.%). Whereas SiO_2 (10 to 16 wt.%) is at a similar concentration as in the sediment-hosted coffinite, vein coffinite contains only half the UO_2, ~32 wt.%. Thorium oxide reaches on average 0.3 wt.%. It has high 9 to 14 wt.% Y_2O_3, but very little ~0.08 wt.% Ce_2O_3, indicating strong relative enrichment of heavy rare earth elements (HREE) over light rare earth elements (LREE). CaO ~1.8 wt.% is like the sediment coffinite. Contamination with Fe is slightly higher at ~1.2 wt.%.

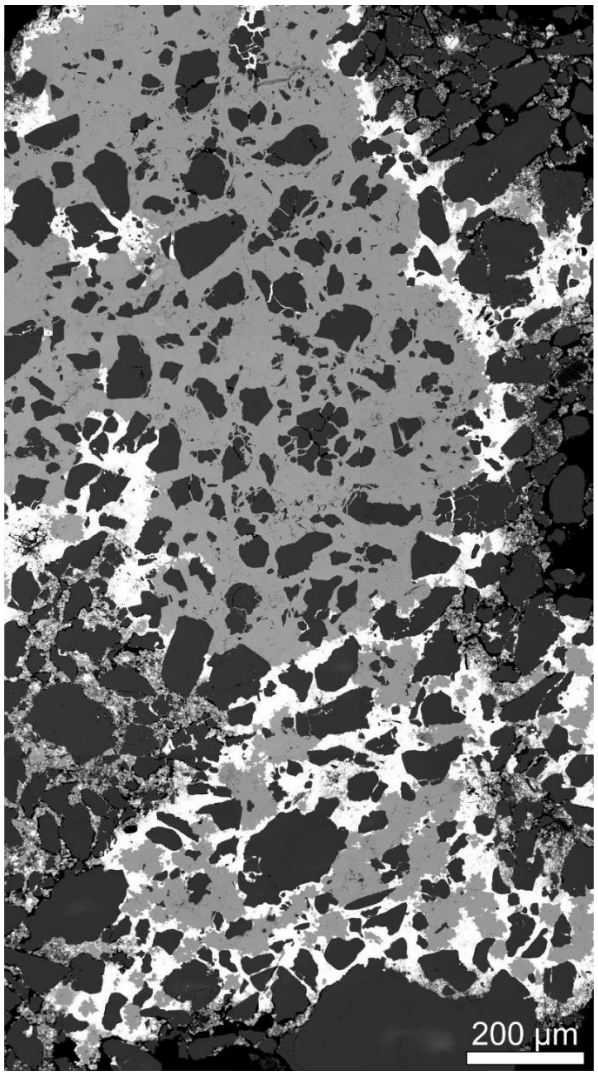

Figure 6. Backscatter electron image of a pyrite nodule. Bright—coffinite; grey—pyrite; dark—quartz.

Saprolite-hosted coffinite is distinctly ThO_2-rich, but the content is highly variable between 1.8 and 12 wt.%. Elements can be roughly separated into two groups. UO_2 and Ce_2O_3 correlate, while

ThO_2, Y_2O_3, CaO, and P_2O_5 correlate. Considering the spatial association of coffinite and thorite in the saprolite, this is interpreted as coffinite with a considerable thorite component and either the result of strong U(+Ce) enrichment of (magmatic) thorite or mobility of Th(+Ca,Y,P) over several µm, resulting in deposition of high-Th coffinite.

This is supported by analyses of high-U thorite in the saprolite, which show very similar trends. ThO_2, Y_2O_3, CaO, and P_2O_5 correlate and are significantly higher, while UO_2 and Ce_2O_3 are lower compared to high-Th coffinite.

Analysed uraninites have low analytical totals (72 to 81 wt.%). They contain 57 to 67 wt.% UO_2, 6 to 16 wt.% SiO_2, ~1.5 wt.% CaO, ~0.5 wt.% Ce_2O_3, ~1.2 wt.% Y_2O_3, and 1.5 to 5.0 wt.% FeO. At first sight, the designation uraninite seems odd, considering that SiO_2 is barely lower compared to the vein coffinite, and UO_2 reaches only the levels observed in sediment-hosted coffinite. Firstly, these analyses are geochemically distinct from endmember coffinite, e.g., by negligible P content. Secondly, all analyses are from grains visually different from coffinite. Thirdly, U, Ce, Y, and Pb correlate, indicating they are contained in the uraninite, while there is no correlation between Si, Fe, and U, indicating that Fe and Si are contamination by quartz and hematite as much as by coffinitisation of uraninite.

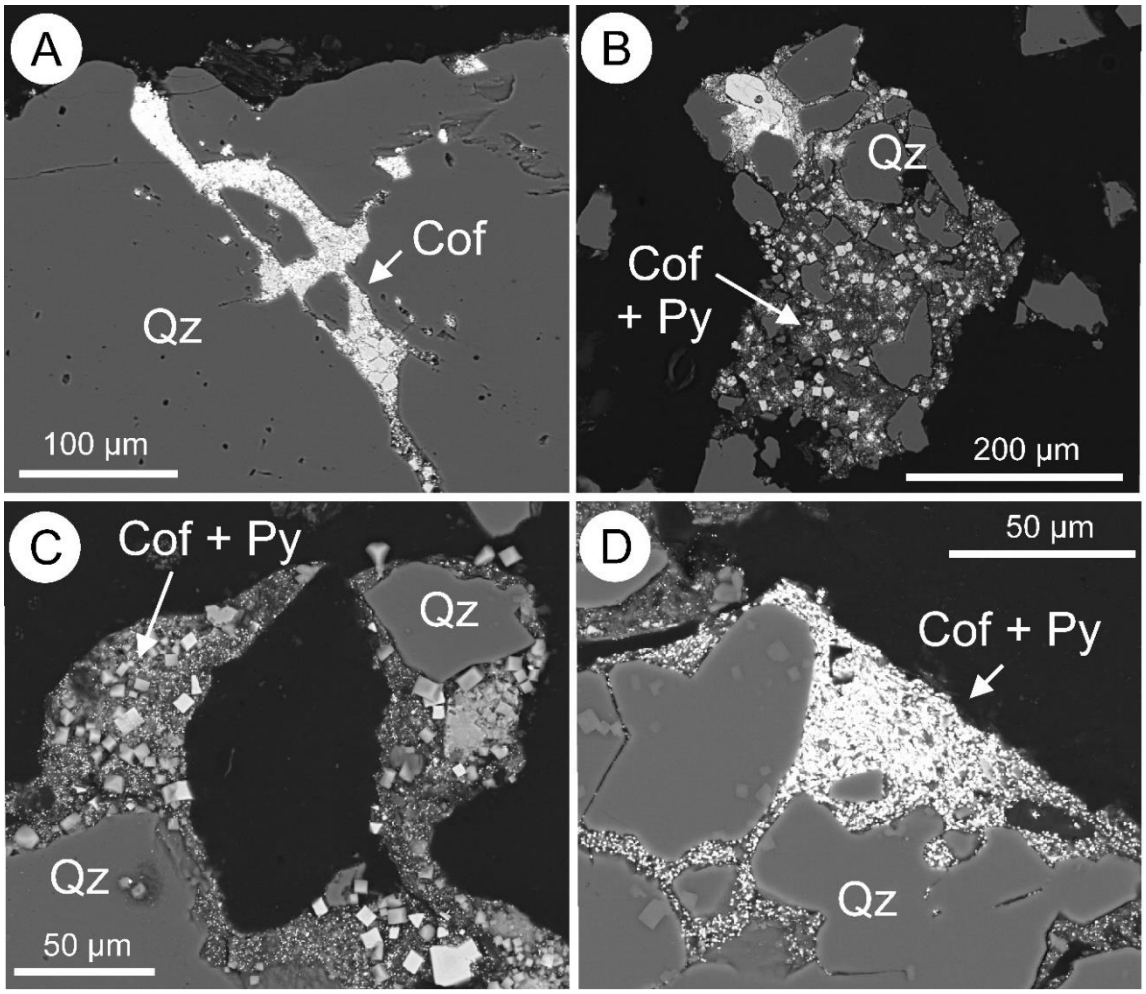

Figure 7. BSE images showing petrographic aspects of uranium mineralisation in sedimentary rocks. (**A**) Micro-crystalline coffinite (Cof) within fractures in quartz (Qz). (**B**) Micrometer-scale coffinite, pyrite (Py) and trace uraninite within fractures and voids in quartz. (**C**) Fine-grained intergrowths of coffinite and pyrite on the margins of quartz. (**D**) Fine-grained intergrowths of coffinite and pyrite within quartz.

4.3. U–Pb Microprobe Dating

The results of chemical U–Pb dating (421 spot analyses) of coffinite in all three occurrences (sandstone, saprolite and veins) are summarised in Figure 8. The resultant histogram shows a normal distribution with a weighted average age of 16.98 ± 0.16 Ma for the whole coffinite population. Uraninite from the granite-hosted vein yielded a significantly older age (40 ± 2 Ma). The full set of geochronological data are provided as Supplementary Materials.

4.3.1. Sediment-Hosted Coffinite

The ages of coffinite in the lignite and pyrite nodules are almost normally distributed between 9 and 22 Ma. The tails on both sides (kurtosis) are slightly too high. Nevertheless, it is a probability distribution and can be readily interpreted as a single event. The weighted average is 16.98 ± 0.16 Ma. The average relative error for individual single points is ~7.2% (~1.2 Ma).

There is no difference in ages or their distribution between samples or between lignite-associated and pyrite-associated coffinite. Ages do not seem affected by low totals, but age errors are usually slightly higher for those analyses due to lower concentrations.

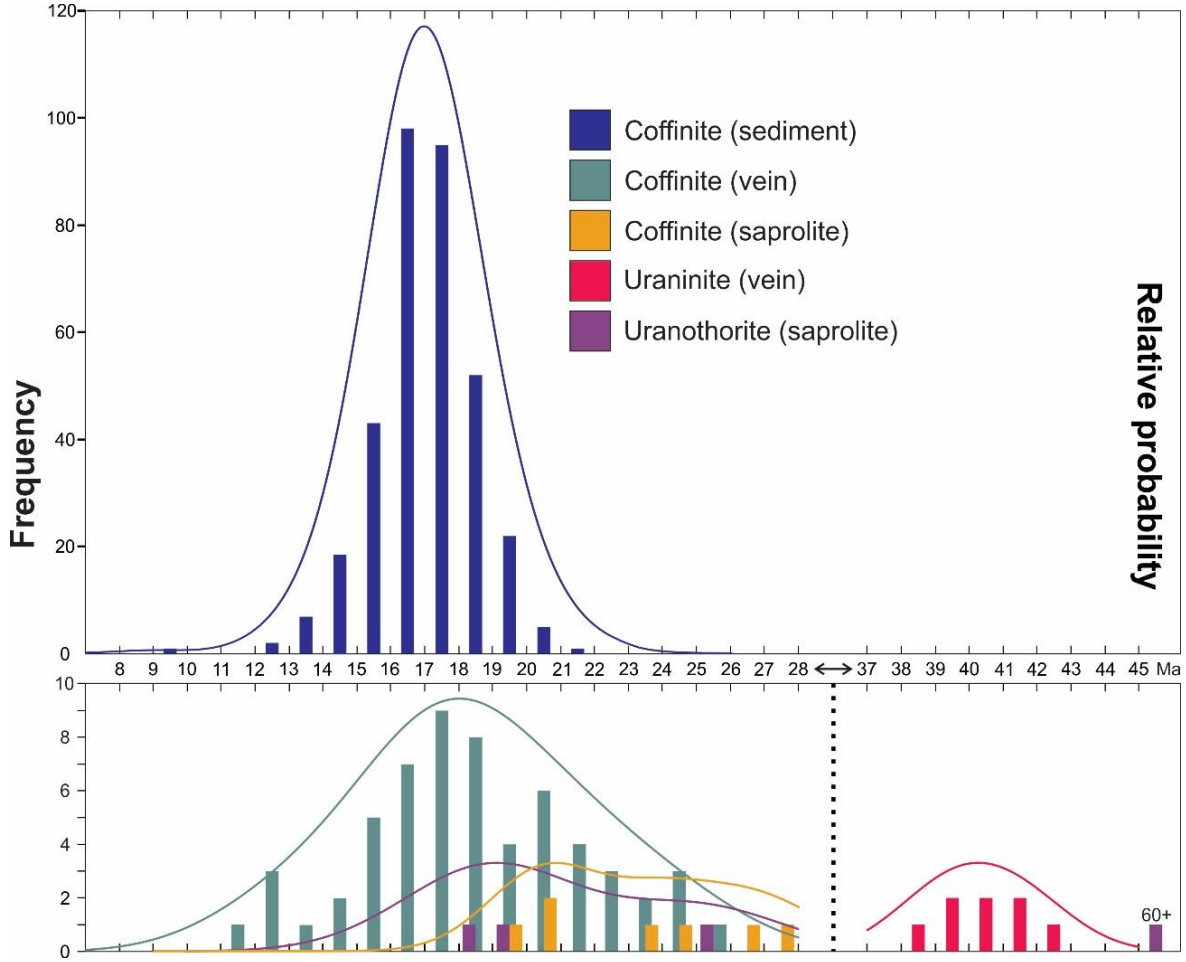

Figure 8. Histogram of obtained ages in Ma with relative probability curves superimposed. Note the normal distribution of coffinite ages.

4.3.2. Saprolite

Dating of *uranothorite* gave ages from 18 to 25 Ma. Lead loss (and thus younger ages) might have been expected but this is not the case, potentially pointing at chemical weathering prior to the

formation of U-minerals. Errors are around ~2.5 Ma for all spots (4 to 14%). These ages are likely the result of (almost) complete isotopic resetting of magmatic thorite.

The Th-rich coffinite yielded ages of 20 Ma to 28 Ma with an average relative error of 7% (~1.6 Ma). The ages are older than those of the sediment-hosted coffinite but are not unexpected considering the likely old, magmatic thorite component. The populations of both species are, however, relatively small and the ages obtained should be treated with caution.

4.3.3. Vein-Hosted Coffinite and Uraninite

Porous coffinite from the vein gave ages from 12 to 25 Ma with an average error of 13% (~2.3 Ma). This is roughly twice the relative error of coffinite analyses in the sediment. The ages show a distribution comparable to the sediment-hosted coffinite although the median is slightly shifted to ~18.5 Ma and the distribution is less symmetrical (Figure 8).

Dating of uraninite from the granite-hosted vein yielded ages of 38 to 42 Ma with an average of 40 Ma. The relative error for single points is ~3% (~1.6 Ma). There is a weak correlation between higher Fe and older age, indicating the addition of Pb by hematite. Considering the generally high Fe in these uraninite analyses, the true age of uraninite is likely lower than 40 Ma, but nevertheless still older than all dated coffinite.

5. Discussion

Precise age dating of sediment-hosted U deposits faces a variety of obstacles. The high permeability of the sediment facilitates mobility and loss of radon (Rn). The longevity of the mineralising system and the ubiquitous presence of groundwater allow for continuous migration of daughter radionuclides, e.g., Rn, Ra and Pb, from parent U. Therefore, dateable minerals like coffinite and uraninite can be considered to display relatively open system behaviour in sediment-hosted U deposits. This can lead to acquired ages rarely representing the time of U deposition. Despite this, loss and gain of elements are unlikely to ever be homogeneous across the system and the ages of minerals are very rarely completely reset. This, in turn, leads to a wide spread of ages over several Ma, or more (e.g., [32]).

The tight range of ages for dense coffinite in the sediment, describing a probability distribution with a single peak at ~17 Ma (Figure 8), can be readily interpreted as unaffected by open system behaviour and thus, would represent valuable evidence for a single coffinite-forming event during the Miocene. The coffinite in the sediment samples is fine-grained and intergrown with pyrite, but importantly, it is non-porous, which likely helped maintain a (relatively) closed system that allowed retention of Rn, Ra, and Pb. It should, however, be mentioned that these samples are possibly not fully representative, given that the main style of U mineralisation in the sediment is porous coatings on quartz grains that cannot be analysed. The ~17 Ma age obtained in this study is therefore subject to a twofold sampling bias. It could be argued that high rates of U precipitation would result in larger crystals, more easily age dated, whereas slower precipitation rates lead to fine-grained intergrowths. Secondly, the selection of very high U sediments for analysis followed by a focus on grains sufficiently large for that analysis could effectively have introduced a biased sampling of U minerals formed during a single event of major U input. In addition, rejecting analyses of highly porous U minerals because of low analytical totals could have removed much of the reset material. Lastly, a degree of open system behaviour is documented by the presence of radionuclides in groundwater at the Blackbush prospect, indicating that the assumption of closed system behaviour may not be entirely correct.

The ages obtained for the porous vein coffinite exemplify the problems mentioned above. Compared to the dense sediment-hosted coffinite, ages show a wider spread and do not follow a normal probability distribution (Figure 8). Aside from the main peak at ~18 Ma, several smaller peaks at ~12, ~20, and 24 Ma are noted. The origin of these ages cannot be resolved in greater detail, and likely do not carry any genetic information. They are the result of an unknown combination of primary coffinite deposition, open system behaviour and resetting, and, considering the presence of older uraninite in the vein, also coffinitisation of uraninite. This alteration process released radiogenic

lead due to the reduced compatibility of Pb in the coffinite structure compared to uraninite (e.g., [25]), which could be deposited on grain surfaces, further skewing the ages of highly porous coffinite.

During the Cainozoic, sedimentary basins in South Australia (Figure 9) went through very similar events and processes, which in turn led to similar suitable conditions for U deposits. In the Pirie Basin, the Eocene organic-rich Kanaka Beds were deposited, contemporaneous with the Maralinga Member in the Eucla Basin and the Eyre Formation in the Lake Eyre Basin, all of which host uranium. The age of the coffinite, ~17 Ma, coincides with the Garford Formation in the Eucla Basin, and Namba Formation in the Southern Callabonna Sub-basin. Still, it is unlikely that sedimentation occurred around 17 Ma which could have controlled coffinite formation, although the exact age of the Melton Limestone has been discussed [6,33].

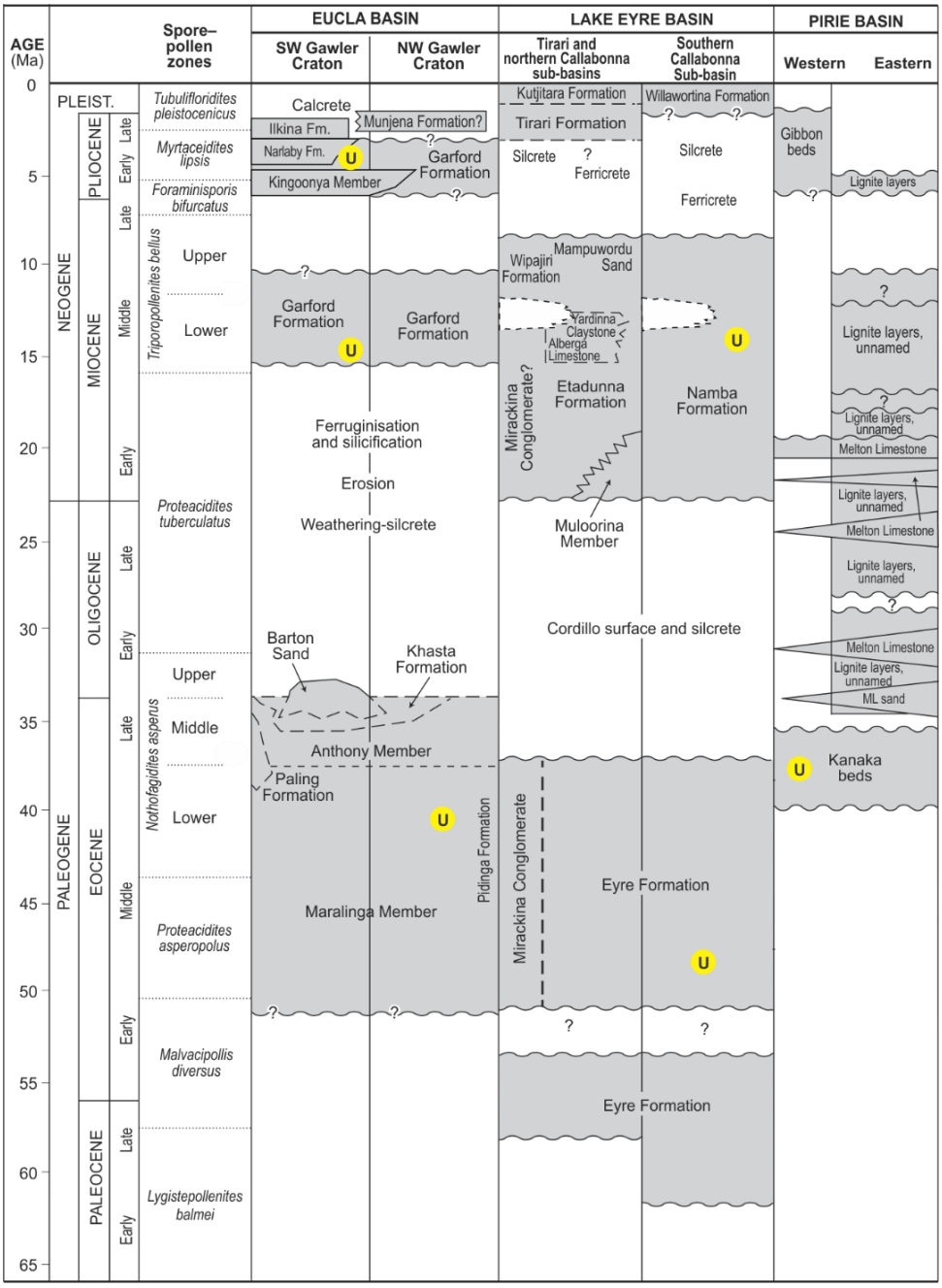

Figure 9. Comparative stratigraphy of Palaeogene-Neogene sedimentary stratigraphy in South Australian basins and adjacent areas. Figure adapted from [6].

While the Garford and Namba Formations are known to host U, the preservation of a unique 17 Ma age, inferring U immobility, is only documented in the Pirie Basin. Dating of U-minerals in other sediment-hosted U deposits in South and Western Australia typically yields young ages, e.g., 6.7 to 3.4 Ma in the Beverley deposit, Lake Frome Basin [34,35], or is unsuccessful or ambiguous due to open behaviour and repeated resetting [32].

An age of ~17 Ma does, however, coincide with the Miocene Climate Optimum [36]. The Eocene and Miocene are characterised by hot and wet climates in Southern Australia, leading to abundant vegetation and, in turn, to organic-rich channel fills. On one hand, hot and wet climates are beneficial for U deposition, e.g., by increased groundwater flow. On the other hand, slow but continuous changes in climate should lead to similarly evolving changes in U deposition, which would result in a more undulating distribution of ages instead of a single peak at 17 Ma.

A variety of vein-hosted U systems of limited size can be found on the eastern edge of the Eyre Peninsula [1]. They are associated with the Kalinjala Mylonite zone (KMZ), a major lithospheric boundary and palaeosuture between two terranes. The Roopena Fault is the northern extension of the KMZ. As mentioned above, subordinate branches of the Roopena Fault cross the prospect. In addition, even though the Roopena and the KMZ are not in direct contact (rather, they are separated by a broader fault splay system) and the Roopena Fault appears to turn south-east into the Spencer Gulf, an inferred connection between them places the lithospheric boundary very close to the Blackbush prospect. The increased level of fracturing and veining of the granite closer to the U mineralisation further supports the strong influence of fractures and fluid movement along them. The most likely explanation for the ~17 Ma age is the triggering of U-rich fluids by tectonic movement along this lithospheric boundary.

Other vein-hosted uranium mineralisation in South Australia does not have a clear source, whereas observed relationships suggest that the Blackbush prospect likely sources its U from the underlying high-U granite. The vast difference in size between them, e.g., the Hospital Prospect, Port Lincoln (5 tonnes U [37]) compared to Blackbush (12,500 tonnes U), could indicate that simple leaching of U from the basement by groundwater is a significant mechanism.

The saprolite investigated here yielded far fewer U minerals than had been expected from logs provided by UraniumSA. It remains unclear whether much U was lost during processing, or alternatively if U is instead adsorbed onto clay minerals. The distinct Th-rich character of the coffinite indicates that this is not likely representative for the mineralisation of the saprolite, and rather it is a highly U enriched magmatic thorite.

The significantly older age for the granite-hosted vein uraninite indicates this predates sedimentation of the Eocene Kanaka Beds. Quartz dissolution is greatly facilitated by organic acids, which in turn supports the precipitation of coffinite, hence it is the only U mineral in the organic-rich sediment. The presence of uraninite could indicate transport and redeposition of uranium by meteoric fluids within the exposed granite. If the uraninite predates sedimentation of the Kanaka Beds, it would indicate that (true) groundwater is unnecessary for U transport.

6. Implications and Conclusions

Coffinite ages define an almost perfect normal distribution suggestive of a single coffinite-forming event at ~17 Ma, likely triggered by tectonic movement along a major lithospheric boundary. Uncertainties remain, however, about the proportion of U brought in the system during the event, compared to simple leaching of U from the basement by groundwater. Age constraints from coffinite in the saprolite (28–20 Ma) are based on fewer analyses and, in all probability, represent incomplete resetting of older *uranothorite*. Uraninite in granite-hosted veins gives an age of 42–38 Ma. Uranium mobility would appear to predate sedimentation of the preserved cover sequence. The ages obtained here on hydrothermal minerals support a conceptual genetic model in which tectonic movement along the reactivated Roopena Fault triggered the flow of U-rich fluids into the cover sequence

The new data will assist with the optimisation of exploration strategies seeking to identify additional uranium resources in the region [38], even if some of the interpretations reached here may

suggest that Blackbush may have formed where it is due to a combination of favourable factors that may not be widely repeated. The petrographic work detailed here on the nature of the uranium minerals represents valuable background information that may assist in the eventual exploitation of the Blackbush resource, e.g., by in situ leaching.

Supplementary Materials: The following are available online at http://www.mdpi.com/2075-163X/10/2/191/s1, EPMA dataset for the analysed U minerals.

Author Contributions: U.D. and N.J.C. wrote this paper. U.D. and B.P.W. performed the analytical work, including the microprobe U–Pb dating. Data processing was carried out by U.D. and B.P.W., assisted by L.C.-D.). The project was devised by N.J.C. and R.B. and supervised by N.J.C and C.L.C. All authors have read and agreed to the published version of the manuscript.

Funding: U.D. acknowledges receipt of a Ph.D. scholarship from the Carthew Family Trust from which this project was funded. N.J.C. acknowledges additional support from the ARC Research Hub for Australian Copper-Uranium (Grant IH130200033).

Acknowledgments: We appreciate the constructive comments of Nicole Hurtig and two anonymous reviewers, which helped us improve clarity and presentation.

Conflicts of Interest: The authors declare no conflicts of interest.

References

1. Wilson, T. *Uranium and Uranium Mineral Systems in South Australia*, 3rd ed.; Report Book 2015/00011; Geological Survey of South Australia, Mineral and Energy Resources Group: Adelaide, Australia, 2015; p. 191.
2. Hitzman, M.W.; Valenta, R.K. Uranium in iron oxide-copper-gold (IOCG) systems. *Econ. Geol.* **2005**, *100*, 1657–1661. [CrossRef]
3. Skirrow, R.; Bastrakov, E.N.; Barovich, K.; Fraser, G.L.; Creaser, R.A.; Fanning, C.M.; Raymond, O.L.; Davidson, G.J. Timing of Iron Oxide Copper-Gold Hydrothermal Activity and Nd Isotope Constraints on Metal Sources in the Gawler Craton, South Australia. *Econ. Geol.* **2007**, *102*, 1441–1470. [CrossRef]
4. Ehrig, K.; McPhie, J.; Kamenetsky, V. Geology and mineralogical zonation of the Olympic Dam iron oxide Cu–U–Au–Ag deposit, South Australia. In *Geology and Genesis of Major Copper Deposits and Districts of the World, a Tribute to Richard Sillitoe*; Hedenquist, J.W., Harris, M., Camus, F., Eds.; SEG Special Publcation: Lyttelton, CO, USA, 2012; Volume 16, pp. 237–268.
5. Stewart, K.P.; Foden, J. *Mesoproterozoic Granites of South Australia*; Report Book, 2003/15; Department of Primary Industries and Resources, Government of South Australia: Adelaide, Australia, 2003.
6. Hou, B.; Fabris, A.J.; Michaelsen, B.H.; Katona, L.F.; Keeling, J.L.; Stoian, L.; Wilson, T.C.; Fairclough, M.C.; Cowley, W.M. Paleodrainage and Cenozoic coastal barriers of South Australia: A new map and GIS dataset. *MESA J.* **2012**, *66*, 26–32.
7. UraniumSA. Uranium Discovery; ASX Release 12 December 2007. Available online: https://www.asx.com.au/asxpdf/20071212/pdf/316fq84dlcgmsd.pdf (accessed on 19 February 2020).
8. Domnick, U.; Cook, N.J.; Bluck, R.; Brown, C.; Ciobanu, C.L. Petrography and geochemistry of granitoids from the Samphire Pluton, South Australia: Implications for uranium mineralisation in overlying sediments. *Lithos* **2018**, *300–301*, 1–19. [CrossRef]
9. Bluck, R.; Brown, C. Characterisation of the Samphire granite, Hiltaba Suite, northeastern Eyre Peninsula. *MESA J.* **2017**, *85*, 31–40.
10. Cuney, M. The extreme diversity of uranium deposits. *Mineral. Depos.* **2009**, *44*, 3–9. [CrossRef]
11. Bowles, J.F.W. Age dating of individual grains of uraninite in rocks from electron microprobe analyses. *Chem. Geol.* **1990**, *83*, 47–53. [CrossRef]
12. Bowles, J.F.W. Age Dating from Electron Microprobe Analyses of U, Th, and Pb: Geological Advantages and Analytical Difficulties. *Microsc. Microanal.* **2015**, *21* (Suppl. 5), 1114–1122. [CrossRef]
13. Domnick, U.; Cook, N.J.; Ciobanu, C.L.; Courtney-Davies, L.; Dmitrijeva, M.; Verdugo-Ihl, M.R.; Xu, J.; Kennedy, A.K.; Bluck, R. New geochronological constraints on the evolution of the Samphire pluton, South Australia. *Precambr. Res.* **2020**, in review.

14. Reid, A.; Jagodzinski, E.; Gerhard, F. Project PGC03–01: Geochronology from the Samphire Uranium Project. In *PACE Geochronology: Results of Collaborative Geochronology Projects 2013–2015*; Report Book 2015/00003; Jagodzinski, E.A., Reid, A.J., Eds.; Department of the Premier and Cabinet: Adelaide, Australia, 2017; pp. 10–28.
15. UraniumSA. Samphire Project Update; ASX Release 27 September 2013. Available online: https://www.asx.com.au/asxpdf/20130927/pdf/42jnqgsn2cqcgg.pdf (accessed on 19 February 2020).
16. Braun, J.-J.; Pagel, M.; Muller, J.-P.; Bilong, P.; Michard, A.; Guillet, B. Cerium anomalies in lateritic profiles. *Geochim. Cosmochim. Acta* **1990**, *54*, 781–795. [CrossRef]
17. Baes, C.F.; Mesmer, R.E. *The Hydrolysis of Cations*; Wiley: Hoboken, NJ, USA, 1976; p. 489.
18. Stoian, L.M. Palynological Analysis of Samples 53448, 2490100, and 2490112. South Australian Resources Information Gateway. 2009. Available online: http://minerals.sarig.sa.gov.au (accessed on 5 November 2019).
19. Curtis, S.; Wade, C. *Stratigraphy of the Lower Gawler Range Volcanics in the Roopena Area, North-Eastern Eyre Peninsula*; Report number: RB 2015/00021; Geological Survey of South Australia: Adelaide, Australia, 2016.
20. Deditius, A.P.; Utsunomiya, S.; Ewing, R.C. The chemical stability of coffinite, $USiO_4{\cdot}nH_2O$; 0 <n <2, associated with organic matter: A case study from Grants uranium region, New Mexico, USA. *Chem. Geol.* **2008**, *251*, 33–49.
21. Armstrong, J.T. Quantitative analysis of silicate and oxide minerals: Comparison of Monte Carlo, ZAF, and φ(ρz) procedures. In *Microbeam Analysis*; Newbury, D.E., Ed.; San Francisco Press: San Francisco, CA, USA, 1988; pp. 239–246.
22. Donovan, J.J.; Tingle, T.N. An Improved Mean Atomic Number Background Correction for Quantitative Microanalysis. *Microsc. Microanal.* **1996**, *1*, 1–7. [CrossRef]
23. Donovan, J.J.; Singer, J.W.; Armstrong, J.T. A new EPMA method for fast trace element analysis in simple matrices. *Am. Mineral.* **2016**, *101*, 1839–1853. [CrossRef]
24. Cross, A.; Jaireth, S.; Rapp, R.; Armstrong, R. Reconnaissance-style EPMA chemical U–Th–Pb dating of uraninite. *Aust. J. Earth Sci.* **2011**, *58*, 675–683. [CrossRef]
25. Macmillan, E.; Cook, N.J.; Ehrig, K.; Pring, A. Chemical and textural interpretation of late-stage coffinite and brannerite from the Olympic Dam IOCG-Ag-U deposit. *Mineral. Mag.* **2017**, *81*, 1323–1366. [CrossRef]
26. Macmillan, E.; Cook, N.J.; Ehrig, K.; Ciobanu, C.L.; Pring, A. Uraninite from the Olympic Dam IOCG-U-Ag deposit: Linking textural and compositional variation to temporal evolution. *Am. Mineral.* **2016**, *101*, 1295–1320. [CrossRef]
27. Syverson, D.D.; Etschmann, B.; Liu, W.; Ram, R.; Mei, Y.; Lanzirotti, T.; Mercadier, J.; Brugger, J. Oxidation state and coordination environment of Pb in U-bearing minerals. *Geochim. Cosmochim. Acta* **2019**, *265*, 109–131. [CrossRef]
28. Montel, J.M.; Foret, S.; Veschambre, M.; Nicollet, C.; Provost, A. Electron microprobe dating of monazite. *Chem. Geol.* **1996**, *131*, 37–53. [CrossRef]
29. Ning, W.; Wang, J.; Xiao, D.; Li, F.; Huang, B.; Fu, D. Electron Probe Microanalysis of Monazite and Its Applications to U–Th–Pb Dating of Geological Samples. *J. Earth Sci.* **2019**, *30*, 952–963. [CrossRef]
30. Sabau, G. Chemical U–Th–Pb geochronology: A precise explicit approximation of the age equation and associated errors. *Geochronometria* **2012**, *39*, 167–179. [CrossRef]
31. Ludwig, K.R. User's Manual for Isoplot 3.75. *Berkeley Geochronol. Cent. Spec. Publ.* **2012**, *5*, 75.
32. Douglas, G.B.; Butt, C.R.M.; Gray, D.J. Geology, geochemistry and mineralogy of the lignite-hosted Ambassador palaeochannel uranium and multi-element deposit, Gunbarrel Basin, Western Australia. *Mineral. Depos.* **2011**, *46*, 761–787. [CrossRef]
33. McAvaney, S.O.; Wade, C.E.; Krapf, C.B.E. *Geology of the CULTANA 1:100 000 Map Sheet (6432)*; Report Book 2014/00006; Department for Manufacturing, Innovation, Trade, Resources and Energy: Adelaide, Australia, 2014.
34. Wülser, P.-A. Uranium Metallogeny in the North Flinders Ranges Region of South Australia. Unpublished. Ph.D. Thesis, University of Adelaide, Adelaide, Australia, 2009.
35. Wülser, P.-A.; Brugger, J.; Foden, J.; Pfeifer, H.-R. The sandstone-hosted Beverley uranium deposit, Lake Frome Basin, South Australia: Mineralogy, geochemistry, and a time-constrained model for its genesis. *Econ. Geol.* **2011**, *106*, 835–867. [CrossRef]
36. Herold, N.; Huber, M.; Greenwood, D.R.; Müller, R.D.; Seton, M. Early to Middle Miocene monsoon climate in Australia. *Geology* **2011**, *39*, 3–6. [CrossRef]

37. King, D.; Woodmansee, W.C. Port Lincoln Uranium Exploration—Diamond drilling at the Hospital Prospect. In *Mining Review*; South Australia Department of Mines: Adelaide, Australia, 1956; Volume 101, pp. 32–41.
38. Hou, B.; Keeling, J.; Li, Z. Paleovalley-related uranium deposits in Australia and China: A review of geological and exploration models and methods. *Ore Geol. Rev.* **2017**, *88*, 201–234. [CrossRef]

© 2020 by the authors. Licensee MDPI, Basel, Switzerland. This article is an open access article distributed under the terms and conditions of the Creative Commons Attribution (CC BY) license (http://creativecommons.org/licenses/by/4.0/).